Initiation of Internal Erosion in Earth Dams: A Particle-Scale Computational Approach

J. Qi[1], N. Yousefpour[2], PhD, PE, G. Narsilio[3], PhD, and M. Pouragha[4], PhD

[1]PhD Student, The University of Melbourne, Department of Infrastructure Engineering, Parkville, VIC; email: jie.qi@student.unimelb.edu.au
[2]Doreen Thomas Fellow, The University of Melbourne, Department of Infrastructure Engineering, Parkville, VIC; email: negin.yousefpour@unimelb.edu.au
[3]Professor, The University of Melbourne, Department of Infrastructure Engineering, Parkville, VIC; email: narsilio@unimelb.edu.au
[4]Assistant Professor, Carleton University, Department of Civil and Environmental Engineering, Ottawa, CA; email: MehdiPouragha@cunet.carleton.ca

ABSTRACT

Australia is known as the driest populated continent in the world, but with periods of high rainfall and flooding followed by long droughts. Earth dams are the number one supplier of water for irrigation, hydropower, and clean water, as well as the major infrastructures for flood control, amongst other purposes. Internal erosion accounts for about 50 percent of dam failures in Australia and across the world. Such failures could be catastrophic, as they often occur without noticeable precursors, posing significant risks to public safety and downstream infrastructures. In this study, we incorporate the Discrete Element Method (DEM) coupled with Computational Fluid Dynamics (CFD) to simulate soil samples under internal erosion as representative elements for dams. The outputs of simulations are evaluated using a statistical machine learning (ML) method to better assess the triggers of internal erosion based on spatiotemporal patterns in particle-scale and sample-scale parameters, such as particle velocity, particle-particle contact force, and fluid-particle coupling force, as well as kinetic and total energy during the initiation of erosion process. Understanding these patterns and correlations at the particle scale may assist in (macro-scale) engineering monitoring and mitigation strategies.

Keywords: DEM-CFD, AI-ML, Internal Erosion, Early Detection, Initiation, Earth Dams

1 INTRODUCTION

Internal erosion is a typical issue faced by water-retaining structures such as earth dams, posing a significant risk to public safety and the economy. This phenomenon frequently occurs in gap-graded soils subjected to certain hydraulic and mechanical conditions. In this context, the internal erosion in structures such as earth dams has been studied through different methods, such as field monitoring (Chen et al. 2018; Cai et al. 2020), laboratory tests, including triaxial sample tests (Richards et al. 2012; Fonseca et al. 2014) and model tests (Planès et al. 2016), as well as numerical simulations (Wang et al. 2017; Zou et al. 2020). The initiation and development of internal erosion are mainly influenced by three factors: (a) particle gradation, (b) hydraulic condition, and (c) mechanical state (Brown et al. 2009). Internal erosion usually initiates from imperceptible transport of fine particles at the pore scale with no evident signs and gradually develops into catastrophic dam breaches, which makes the early detection of internal erosion an essential demand.

The development of numerical simulation and data-driven tools such as machine learning has made it possible to gain insights into the initiation of internal erosion at the particle scale. In this research, we developed a 3D coupled Computational Fluid Dynamics (CFD) - Discrete Element Method (DEM) model of gap-graded sand samples. The relative density and small strain stiffness of the model are calibrated with a virtual simple shear test combined with empirical equations. The CFD-DEM model is subjected to a hydraulic gradient that prompts internal erosion. Some particle-scale parameters (e.g., particle velocity, particle-particle contact force, particle-fluid coupling force, particle contact number) and sample-scale parameters (e.g., mass loss), are monitored. A statistical machine learning (ML) approach using the Ridge Regression method is taken to provide particle-scale insights from the data and reveal the subtle patterns indicating the initiation of internal erosion.

2 NUMERICAL MODEL

2.1 Particle gradation and calibration

A gap-graded sand sample with Fine Content (FC) of 25% is selected for the simulation (the fine content is still sand with diameters of 0.363 mm and 0.30 mm). The gradation curve of the sand sample is shown in Figure 1. The 2 groups of coarse particles with diameters of 3.43 mm and 2.36 mm make up 37.5% of the total mass, while the 2 groups of fine particles represent 12.5% of the total mass respectively (Table 1).

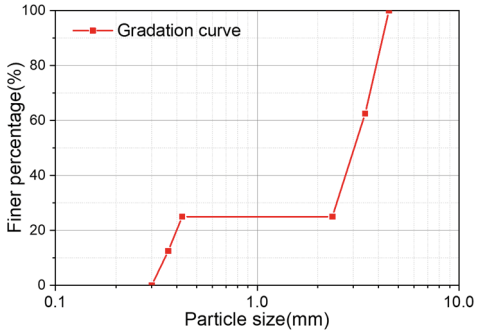

Figure 1. Particle gradation curve

Table 1. Particle size and mass fractions

Particle Group	Diameter [mm]	Relative Diameter	Mass Fraction [%]
D1	3.43	1.000	37.5%
D2	2.36	0.688	37.5%
D3	0.363	0.106	12.5%
D4	0.30	0.087	12.5%

The calibration of the DEM assembly is conducted in virtual simple shear tests. The Hertz-Mindlin model is adopted for particle-particle and particle-wall contacts. The NGI-type simple shear model with stacked rings is adopted following the numerical model of Asadzadeh et al. (2016). The assemblies are generated in a cylindrical chamber confined by 10 rigid rings with a diameter of 70 mm and a height of 20 mm. A vertical load FN is applied to the top plate of the model to compact the sample. During the simple shearing test, a horizontal velocity of 0.1 mm/s is assigned to the bottom plate while that of the top plate is fixed to 0, such that the horizontal velocity of the rings increases from 0 on the top to 0.1 mm/s on the bottom.

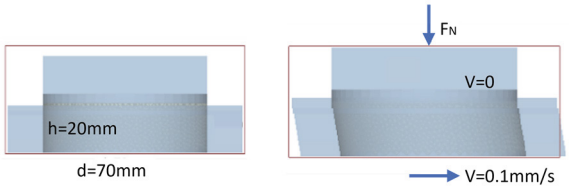

Figure 2. Simple shear test calibration model

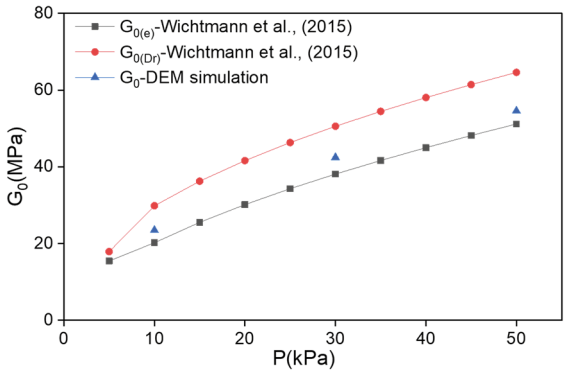

Figure 3. Prediction of G_0 with empirical equations

Table 2. Calibration model parameters

Particle properties		Particle-particle contact		Particle-wall contact	
$\rho_{partcile}$	2650 kg/m^3	μ	0.75	μ	0
E	1e8Pa	μ_r	0.3	μ_r	0
v	0.25	C_{res}	0.2	C_{res}	0.2
D_r	0.51	n	0.33		

Particle density $\rho_{particle}$; Young Modulus E; Poisson's ratio v; Coefficient of static friction μ: the ratio of static friction force to normal contact force; Coefficient of rolling friction μ_r: the ratio of rolling resistance force to normal contact force; Restitution coefficient C_{res}: ratio of relative velocity after colliding to initial relative velocity; Relative density Dr; and Porosity n.

The small strain stiffness G_0 from simple shear tests is compared with that of the empirical equations proposed by Wichtmann et al. (2015) which consider the impact of gradation and fine content (Figure 3). The $G_{0(e)}$ and $G_{0(Dr)}$ are the small strain stiffness from experiential equations based on void ratio e and relative density Dr. While obtaining G_0 from a simple shear test on anisotropic material involves errors, the measurement taken herein is to serve as a first-order approximation of the elastic stiffness. The results from the calibrated model show good agreement with the empirical formula. The calibration model parameters are summarised in Table 2 with the Young's Modulus of the particles limited to 1e8 Pa to save the computational resources (Asadzadeh et al. 2016).

2.2 CFD-DEM model

The CFD-DEM model of the gap-graded sand is created in a cylinder wall (D=15mm, H=25 mm as in Figure 4) with the same gradation (Figure 1), mass fraction (Table 1), and particle parameters (Table 2) as the calibration model. The time step of DEM is set to be 5e-7 s for the stability of calculation. For the first step, the particles are randomly generated at the top of the cylinder with predefined mass fractions (Table 1) and then settled to the bottom under gravity. After the generated particles settle down, the density of the loose sample is measured as the minimum density. To calculate the relative density, the static and rolling friction coefficients of the particle are set to 0 to achieve the dense state with maximum density. Based on the estimated minimum and maximum densities, the required density of the assembly is then calculated based on the target relative density of the sample Dr. The generated dry samples are then compacted by a plate from the top to achieve the calculated target density.

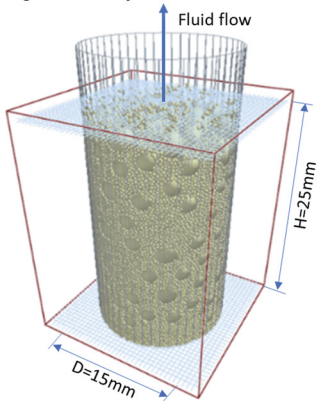

Figure 4. Dimensions of gap-graded DEM sample

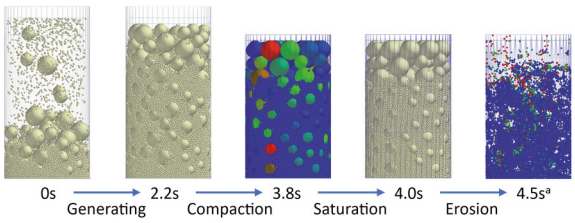

Figure 5. Sample generating and testing
[a] Coarse particles are hidden at t=4.5 s for better visualization

The Finite Volume Method (FVM) is utilized to model the fluid field. The fluid cylindrical domain has the same radius as the DEM assembly, with a larger height to enclose the top and bottom of the DEM sample. Inlet and outlet boundary conditions are assigned to the bottom and top of the fluid field respectively, while the cylinder surface is set as the wall boundary.

The particle-fluid coupling is achieved through solving locally averaged Navier-Stokes (N-S) Equations with the volume fraction ε of the liquid phase calculated in each cell as shown below (Li et al. 2012):

$$\frac{\partial(\varepsilon\rho)}{\partial t}+\nabla\cdot(\varepsilon\rho\mathbf{u})=0 \quad (1)$$

$$\frac{\partial(\varepsilon\rho\mathbf{u})}{\partial t}+\nabla\cdot(\varepsilon\rho\mathbf{u}\cdot\mathbf{u})=-\nabla p+\nabla\cdot(\eta\varepsilon\nabla\mathbf{u})-\varepsilon\rho\mathbf{g}-\mathbf{S} \quad (2)$$

where ε is the volume fraction of fluid; ρ is the fluid density, ρ=1000 kg/m^3; t is time; **u** is the fluid velocity vector; η is the fluid viscosity, η=0.001003 Pa·s, p is the pressure; **g** is the gravity vector, and **S** is the momentum sink.

Force and momentum exchange between the solid and fluid phases is then calculated. The fluid cells are set to be coarser than the largest particle size to avoid 0 values for ε which can cause errors in locally averaged N-S equations. The time step for fluid calculation and information exchange between two phases is 5e-5 s for calculation stability.

The compacted dry sample is then coupled with CFD under static hydraulic pressure for saturation. Both the DEM and CFD simulations continue to reach equilibrium during the saturation process while keeping Dr constant. For the erosion stage, the plate on the top is replaced by a mesh that is only permeable to the fine particles. The hydraulic pressure of the outlet is set to 0, while that of the inlet is fixed to a value that gives a hydraulic gradient of 1 on the whole sample. The fine particles are then eroded from the pore space of coarse particles driven by the hydraulic gradient. The eroded particles are deleted when they are beyond the red rectangular domain of DEM (Figure 5).

3 RESULTS

3.1 Transport of fine particles

After the application of hydraulic gradient at t=4.0 s, the fluid-particle coupling force increases from the values of buoyancy to a higher and steady value within 0.1s for both D3 and D4 (fine) particles (Figure 6(a)). As expected, the loss of fine particles for the D3 group occurs later than that of D4 (Figure 6(b)), due to its relatively larger mass. The progress of internal erosion is calculated as the ratio between the number of eroded particles and the total number (Figure 6(c)). The progress of internal erosion based on lost particles happened after 4.1 s for both groups. However, the erosion in D4 group (fine) particles starts earlier and progresses faster than that of D3. This is also caused by the difference in particle size and mass between the two groups.

The transport of D4 fine particles in the sample is shown in Figure 7 with the particles coloured by velocity-z(a) and fluid-particle coupling force(b). The velocity distribution of particles at 4.5 s indicates the transport of fine particles with an increased rate at the top of the sample. The values of coupling force are dispersed to some extent as the porosity calculated in different fluid cells varies. This mechanism may be the reason the transport of neighbouring fine particles shows different patterns.

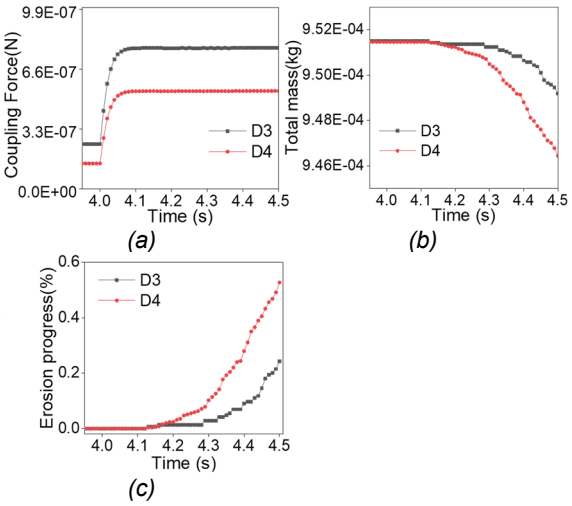

Figure 6. Evolution of averaged particle parameters (a) fluid-particle coupling force of D3 and D4; (b) particle total mass of D3 and D4 (c) erosion progress of D3 and D4

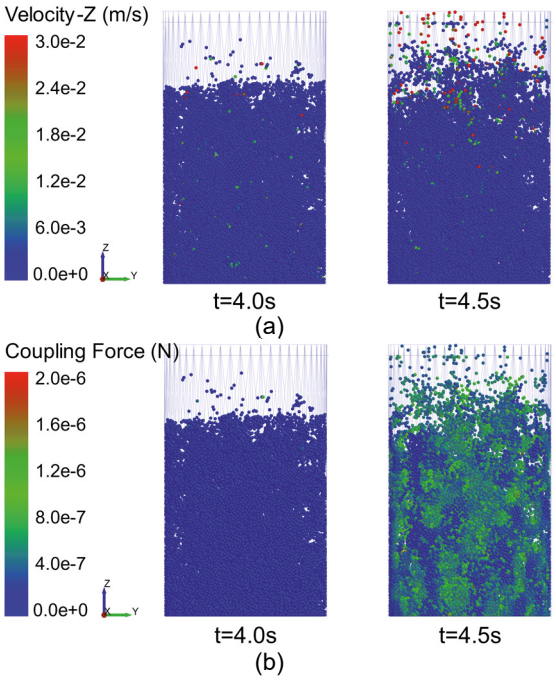

Figure 7. Transport of D4 fine particles (a) particle velocity-z distribution; (b) fluid-particle interaction force distribution

3.2 Evolution of particle-scale parameters

The coordination number quantifies the number of contacts between the target particle and the adjacent ones. After the application of hydraulic gradient, the average coordination number sharply dropped for both D3 and D4 fine particles (Figure 8(a)). The average contact numbers gradually converged to a steady value, which is consistent with the observation of Kawano et al. (2017). The zero-contact ratio of the fine particles is calculated from the ratio of the particles with zero contact numbers over the total number of particles remained within the sample in that group (i.e., total number of particles - number of eroded particles). Both the zero-contact ratio of the D3 and D4 group of fine particles sharply increased after t=4.0 s and then decreased to a relatively low value. The peak of D4 is higher than that of D3, as expected, as the finer particles are subjected to a higher rate of erosion.

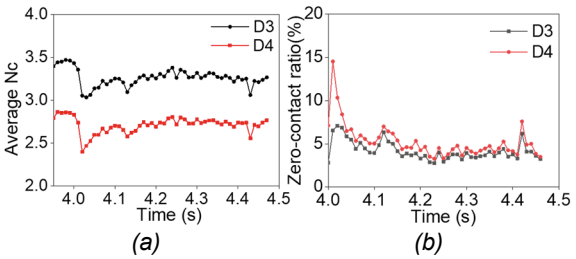

Figure 8. Evolution of particle contact state (a) average coordination number of D3 and D4; (b) zero contact ratio of D3 and D4

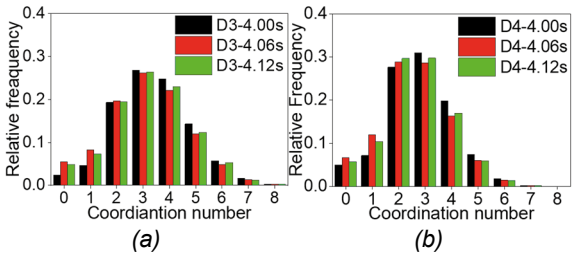

Figure 9. Statistical distribution of particle coordination number (a) D3 group fine particles (b) D4 group fine particles

The statistical distribution of particle coordination numbers for the D3 and D4 group fine particles at t=4.00 s, t=4.06 s, and t=4.12 s are shown in Figure 9. The relative frequency of low coordination numbers at both t=4.06 s and t=4.12 s increased compared with that of t=4.00 s. This indicates more particles lost contact with adjacent particles and started to be eroded from the sample. The decrease of coordination number can be a parameter indicating the initiation of internal erosion at the particle scale.

3.3 Assessment of particle-scale parameters on internal erosion

The particle-scale parameters could reveal the initiation of internal erosion. However, due to the large number of particles and the associated parameters, plus their temporal variations and interactions among them, it is challenging to understand the embedded internal erosion patterns and make interpretations directly from the data. Therefore, we have applied statistical machine learning to analyse the particle-scale behaviours associated with the initiation of internal erosion. For this analysis, the particle-scale parameters of the D4 group are incorporated throughout the erosion process (from 4.0 s to 4.5 s) with a time resolution of 0.01 s, including 13 parameters associated with 23,200 fine particles incorporated (Table 3).

The scikit-learning library (Pedregosa et al. 2011) is utilized to calculate the importance of the particle-scale parameters through Ridge regression approach. The decrease of coordination number at each time step is used as a measure of internal erosion and is defined as the response (target) variable in equation (3). The 13 particle-scale parameters for all the D4 particles are considered as the predictor variables forming the 13 x 23200 matrix in equation (4). The ridge regression is then used to fit the multiple-linear regression model between the predictors, $X_{(t,k,n)}$ and the response variable, $y_{(t,n)}$ at each time step, t throughout the simulation. All the variables are normalized before regression:

$$y_{(t,\,n)}=N_{\mathbf{c}(t_0=4.0,n)}-N_{\mathbf{c}(t,\,n)} \quad (3)$$

$$X_{(t,k,n)}=\begin{bmatrix} X_{(t,k=1,n=1)} & \cdots & X_{(t,k=13,n=1)} \\ \vdots & \ddots & \vdots \\ X_{(t,k=1,n=23200)} & \cdots & X_{(t,k=13,n=23200)} \end{bmatrix} \quad (4)$$

$$y_{(t,n)}=X_{(t,k,n)}\cdot\mathbf{B}_{(t,k)}+e_{(t,k)} \quad (5)$$

where $t\in\{4.01, 4.02\cdots4.50\ s\}$; $k\in\{1, 2\cdots13\}$ is the ID of particle-scale parameters; $n\in\{1, 2\cdots23200\}$ is the fine particle ID number; $N_{\mathbf{c}(t,n)}$ is the coordination number of particle number n at time step t; $y_{(t,n)}$ is the decrease of coordination number for the n'th particle at time step t; $X_{(t,k,n)}$ is the k'th parameter of the n'th particle at time step t; $\mathbf{B}_{(t,k)}$ and $e_{(t,k)}$ are regression coefficients and errors of the ridge regression.

The regression coefficients are then evaluated to compare the contribution of each particle-scale parameter to the decrease of coordination numbers. The importance coefficients of the parameters are ranked based on averaged regression coefficients throughout the time steps (Figure 10). The particle velocity magnitude (X7) and kinetic energy (X8) are the most important parameters influencing the reduction of coordination numbers (parameters that are directly related to the transport of fine particles). The particle-particle contact force (X11) is another essential parameter, as the contact forces from adjacent particles restrict the floating of the target particle. Based on the results of the regression, the total energy (X10) is another important factor contributing to erosion. The potential energy of particles is mainly determined by their Z-position, which makes it show similar importance as the particle position on the Z-axis (X3).

The evolvement of the importance coefficient for the four most significant parameters (X7, X8, X10, X11) together with fluid-particle coupling force throughout the simulation time steps are shown in Figure 11. The fluid-particle coupling force (X12) has a non-negligible influence on the reduction of coordination numbers at the beginning; however, it shows no significant influence for the rest of the time. This is because the fluid-particle coupling force disturbed the initial mechanical balance of fine particles. The mechanical and dynamic response of fine particles then causes the drop of coordination number in Figure 8(a), when the coupling force keeps relatively stable (Figure 6a)) hence its low importance coefficient thereafter. The temporal trend of the coefficients for the top 4 important parameters shows similarities; they slightly increase at the start of erosion (4.0 s ~ 4.02 s) and sharply fluctuate after t=4.1 s. This might be caused by the interaction between fine particles driven by fluid flow and the skeleton of coarse particles.

Table 3. Particle-scale parameters used to define the D4 fine particles

ID	Parameter	Units
X1	X: Particle Position X	mm
X2	Y: Particle Position Y	mm
X3	Z: Particle Position Z	mm
X4	V_X: Particle Velocity X-component	mm/s
X5	V_Y: Particle Velocity Y-component	mm/s
X6	V_Z: Particle Velocity Z-component	mm/s
X7	V_M: Particle Velocity Magnitude	mm/s
X8	E_K: Particle Kinetic Energy	J
X9	E_P: Particle Potential Energy	J
X10	E_T: Particle Total Energy	J
X11	$F_{P\text{-}P}$: Particle-Particle Compressive Force	N
X12	$F_{F\text{-}P}$: Fluid-Particle Coupling Force	N
X13	D_Z: Z-Displacement	mm

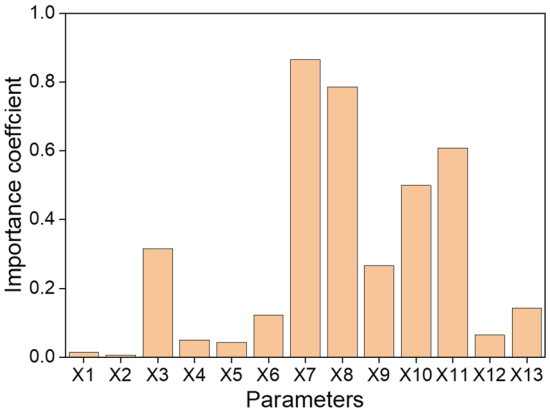

Figure 10. Parameter average importance coefficients

The average values together with confidence intervals of particle-scale parameters from D4 particles are shown in Figure 12. Both the velocity and kinetic energy sharply increase at the initial stage and gradually settle to a lower value with considerable fluctuations. This might be caused by the sudden application of the hydraulic gradient on the sample. The total energy of the particles gradually increases and approaches a relatively stable value as both the increase of particle velocity and z-position (gravitational potential energy) contribute to the total energy. The particle-particle contact force decreases throughout the time steps. The trend shown in Figure 12(a) and (b) is consistent with that in Figure 8 as both the increase-decrease stage and fluctuation stage appear at roughly the same period. The fluctuation stage in Figure 11 also shows a similar trend as in Figure 8 and Figure 12. This similarity reveals the hydraulic gradient is the main influencing factor at the very beginning, while the interaction between fine-and coarse particles contributes more to the fluctuation stage.

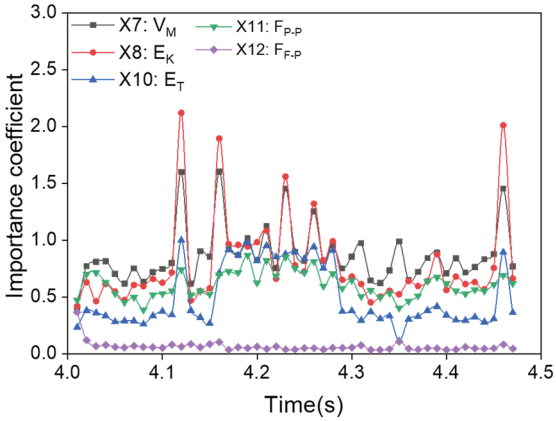

Figure 11. The evolvement of parameter importance coefficients

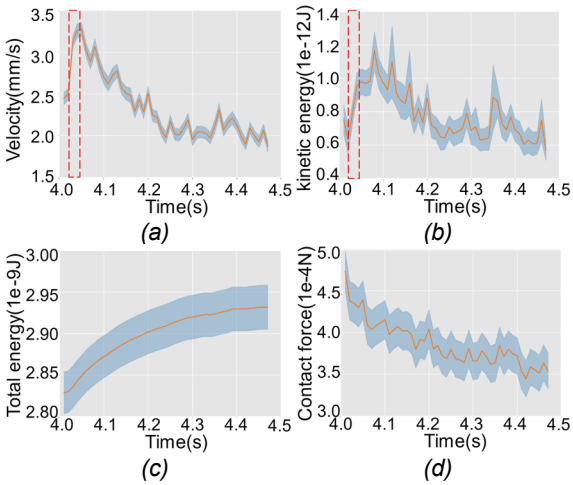

Figure 12. Development of significant parameters(a) particle velocity magnitude V_M; (b) particle kinetic energy E_K; (c) particle total energy E_T; (d) particle-particle compressive force $F_{P\text{-}P}$

3.4 Analysis of internal erosion initiation

The transport of fine particles happened throughout the sample, but higher velocities were observed at top of the sample where the mesh sits. The average coordination numbers of both D3 and D4 group particles deceased shortly after the application of the hydraulic gradient and gradually recovered to a steady value and the relative frequency at low coordination

numbers increased after the hydraulic gradient was applied, showing the internal erosion has started. However, the mass loss did not occur at the initiation of the internal erosion as only when the eroded particles move out of the sample boundary the change of mass could be observed. This indicates that mass loss cannot be used to detect the initiation of internal erosion.

Based on the observation of particle-scale and sample-scale parameters, the internal erosion started shortly after the application of the hydraulic gradient at around t=4.02 s to t=4.0 5 s (4e5~1e6 time steps after applying HG). The considerable decrease of average particle coordination number and the increase of particle velocity both reveal that fine particles are losing contact with other particles and are escaping from the assembly around this time. The gradual recovery of the coordination number shows the disturbance of fine particles caused by the hydraulic gradient fades after t=4.02 s. The fluctuations of the average coordination number after t=4.10 s are mainly due to the mechanical interactions between fine particles and coarse skeletons. This mechanism also caused the fluctuations of particle velocity, particle kinetic energy, and particle-particle contact force after the initiation of internal erosion.

4 CONCLUSION

This research investigates the initiation of internal erosion based on CFD-DEM simulations with a machine learning application. A gap-graded particle assembly is generated with 4 groups of particles of different sizes. A locally averaged CFD-DEM coupling method is utilized to simulate the fluid-particle interactions. Both the sample-scale and particle-scale physical parameters are evaluated to capture the subtle patterns associated with internal erosion.

The mass loss cannot be used to detect the initiation of internal erosion as the erosion starts earlier than the time particles are actually eroded from the sample. This is why the subtle patterns of the particle-scale parameters are more relevant for the assessment of the internal erosion initiation.

The decrease in the coordination number of fine particles is defined as the response variable associated with the internal erosion initiation. Based on the Ridge regression analysis, the particle velocity magnitude, kinetic energy, particle-particle contact force, and particle total energy were found to be the most important particle-scale parameters influencing internal erosion. The fluid-particle coupling force has also shown a non-negligible (but not significant) influence on the initiation of internal erosion. Based on the observation of particle-scale and sample-scale parameters, the internal erosion started shortly after the application of the hydraulic gradient at around t=4.02 s to t=4.05 s. However, the progression of internal erosion based on the loss of particles started after 4.1 s.

Further in-depth analyses using deep learning methods will be performed in the upcoming stages of this research to better identify pattern changes within the particles' mechanistic behaviour at the initiation of erosion to derive more relevant criteria for real-scale evaluation of internal erosion initiation in earth dams.

5 ACKNOWLEDGEMENTS

This research is funded by the University of Melbourne's Early Career Research Grant and complemented by a CSC Scholarship.

REFERENCES

Asadzadeh, M., & Soroush, A. (2016). Fundamental investigation of constant stress simple shear test using DEM. Powder Technology, 292, 129–139.

Brown, A., & Bridle, R. (2009). Report on the European working group on internal erosion, St. Petersburg. Dams and Reservoirs, 19(3), 133–136.

Cai, Y., Cheng, H., Wu, S., Yang, Q., Wang, L., Luan, Y., & Chen, Z. (2020). Breaches of the Baige Barrier Lake: Emergency response and dam breach flood. Science China Technological Sciences, 63(7), 1164–1176.

Chen, C.-Y., Chen, S.-C., Chen, K.-H., & Liu, Z.-H. (2018). Thermal monitoring and analysis of the large-scale field earth-dam breach process. Environmental Monitoring and Assessment, 190(8), 483.

FONSECA, J., SIM, W. W., SHIRE, T., & O'SULLIVAN, C. (2014). Microstructural analysis of sands with varying degrees of internal stability. Géotechnique, 64(5), 405–411.

Kawano, K., Shire, T., & O'Sullivan, C. (2017). Coupled DEM-CFD Analysis of the Initiation of Internal Instability in a Gap-Graded Granular Embankment Filter. EPJ Web of Conferences, 140, 10005.

Li, H., Li, Y., Gao, F., Zhao, Z., & Xu, L. (2012). CFD–DEM simulation of material motion in air-and-screen cleaning device. Computers and Electronics in Agriculture, 88, 111–119.

Pedregosa FABIANPEDREGOSA, F., Michel, V., Grisel OLIVIERGRISEL, O., Blondel, M., Prettenhofer, P., Weiss, R., Vanderplas, J., Cournapeau, D., Pedregosa, F., Varoquaux, G., Gramfort, A., Thirion, B., Grisel, O., Dubourg, V., Passos, A., Brucher, M., Perrot andÉdouardand, M., Duchesnay, andÉdouard, & Duchesnay EDOUARDDUCHESNAY, Fré. (2011). Scikit-learn: Machine Learning in Python Gaël Varoquaux Bertrand Thirion Vincent Dubourg Alexandre Passos PEDREGOSA, VAROQUAUX, GRAMFORT ET AL. Matthieu Perrot. In Journal of Machine Learning Research (Vol. 12).

Planès, T., Mooney, M. A., Rittgers, J. B. R., Parekh, M. L., Behm, M., & Snieder, R. (2016). Time-lapse monitoring of internal erosion in earthen dams and levees using ambient seismic noise. Géotechnique, 66(4), 301–312.

RICHARDS, K. S., & REDDY, K. R. (2012). Experimental investigation of initiation of backward erosion piping in soils. Géotechnique, 62(10), 933–942.

Wang, M., Feng, Y. T., Pande, G. N., Chan, A. H. C., & Zuo, W. X. (2017). Numerical modelling of fluid-induced soil erosion in granular filters using a coupled bonded particle lattice Boltzmann method. Computers and Geotechnics, 82, 134–143.

Wichtmann, T., Navarrete Hernández, M. A., & Triantafyllidis, T. (2015). On the influence of a non-cohesive fines content on small strain stiffness, modulus degradation and damping of quartz sand. Soil Dynamics and Earthquake Engineering, 69, 103–114.

Zou, Y., Chen, C., & Zhang, L. (2020). Simulating Progression of Internal Erosion in Gap-Graded Sandy Gravels Using Coupled CFD-DEM. International Journal of Geomechanics, 20(1).